

A rapid technique for the determination of secondary electron emission yield from complex surfaces

Angelica Ottaviano, Sankha Banerjee,¹ and Yevgeny Raitses¹

¹*Princeton Plasma Physics Laboratory, Princeton, New Jersey 08543, USA*

Abstract

Plasma-wall interaction in the presence of secondary electron emission (SEE) can lead to a degradation and reduction in the performance of plasma devices. Materials with complex surface architectures such as velvet, fuzz, and feathered surfaces have lower SEE yield than the same materials with a flat surface, and can therefore be useful for plasma applications. This reduction in SEE is due to the trapping of secondary electrons in the micro-cavities formed by complex surfaces. In this paper, we present rapid method for a simultaneous comparison of the SEE yield and surface properties of materials with different surface architectures. The method uses Scanning Electron Microscopy (SEM) to simultaneously evaluate the surface morphologies and SEE yield properties for a micro-architected surface. This technique was applied to carbon velvets, and results show agreement with recent theoretical models and with the direct determination of SEE yield from measurements of the currents of the primary electrons impinging the surface and of the secondary electrons emitted from the surface.

Note:

Current affiliation of A. Ottaviano: University of California, Los Angeles

Current affiliation of S. Banerjee: California State University, Fresno

Corresponding author: Yevgeny Raitses, yraitses@pppl.gov

I. Introduction

In plasma applications such as electric propulsion [1-2] and magnetic fusion devices [3-4], the secondary electron emission (SEE) from plasma bounding walls can be an undesired phenomenon causing an enhancement of plasma-wall interactions and increasing power losses in plasma devices [5-7]. Texturing the surface of secondary electron emitting materials with –nano, –micro and even millimeter sized features allows to significantly reduce SEE by trapping and reabsorption of emitted electrons in cavities formed between these features [8-17]. Secondary electrons can either be *true secondary electrons* or backscattered electrons. True secondary electrons originate from the surface atoms of the target material and have energies of up to 50 eV. Backscattered secondary electrons are primary electrons which are either elastically or inelastically backscattered and they have energies between 50 eV and the primary electron energy. In general, the total SEE of a surface is dominated by true secondary electrons [12]. Recent studies have shown that the SEE yield of these complex materials which is defined as the ratio of true secondary electrons to the primary electrons impinging the wall depends on the geometries of their surface structures. For example, in Ref [14], the net SEE yield of a micro-porous Ag surface was reduced by 45% as compared with of the SEE yield from a flat surface made from the same material. This was achieved by controlling the depth and relative placement of the pores with respect to each other. In another case shown in Ref [15], the reduction of SEE yield of a grooved TiN surface is both theoretically simulated and experimentally characterized with respect to the aspect ratio (A_R), which is defined as the ratio of the height to the radius of the groove. In the above examples, the aspect ratio of these materials was typically low ($< 10^2$). In recent studies of higher aspect ratio ($> 10^2$) carbon velvet materials, the SEE yield was reduced up to 65% as compared to a flat graphite surface [1]. In Ref [9], it is predicted that a fractal repeating fibrous structure of a velvet surface

may suppress SEE even more than the high aspect ratio velvet due to the loss of the characteristic angular dependence of the SEE yield on the incident angle of primary electrons. Indeed, for the tungsten fuzz surface, a weaker sensitivity of the SEE yield to the incidence angle of primary electrons was measured as compared to a flat tungsten surface [12]. A strong dependence of the SEE yield on the surface morphology and possible variations and deviations of the actual surface morphology from the designed morphology implies the importance of *in-situ* characterization of the surface structure during the measurements of the SEE properties. In references [10] and [12], a large spread in the local misalignment of fibers from carbon velvets and tungsten fuzz compared with the manufacturing design of the material is observed.

Scanning electron microscopy (SEM) is a widely used tool for the evaluation of the surface structure of materials. Its basic principle of operation is based on the generation of SEE which is registered by an Everhart-Thornley detector [18]. The Everhart-Thornley detector has a scintillator inside a Faraday cage which is biased to different voltages for attracting secondary electrons. A bias of 50 eV is applied to the Faraday cage as to attract true secondary electrons, and backscattered secondary electrons will reach the detector if their direction of travel leads them to it. Therefore, the image signal is generated by mostly true secondary electrons and a fraction of high energy backscattered electrons proportional to the solid angle subtended by the detector. [19] The SEM used in these experiments has a collection angle of 30°. Based on the angular distribution of backscattered electrons described by Lambert's cosine law in Ref [20], the fraction of collected backscattered electrons should be approximately 12%. In addition, the surface composition of the evaluated material can be characterized using energy-dispersive X-ray spectroscopy (EDS) which is an integrated part of many modern SEMs. In the operation of a conventional SEM, a focused electron beam scans the surface of a sample which in turn emits true and backscattered secondary

electrons collected by a detector. The signal generated by the interaction between the primary electrons and the material surface results in a two-dimensional greyscale image of the scanned surface area of the sample [18, 21]. The main advantage of using SEM rather than optical microscopy to image the surface of a material is that its depth of field is very long due to the narrow electron beam which can penetrate far into a sample. These characteristics of SEM are ideally suited for simultaneous characterization of surface morphology and SEE yield from complex surfaces. SEM images were used in a recent study to measure the actual fiber packing density of velvet samples and were compared to measurements of SEE yield of the sample surfaces [10]. These SEE yield measurements are normally made using the current-sample method [10, 12-13, 22], but it should also be possible to use SEM to qualitatively analyze the SEE yield properties of an imaged surface [18]. Methods for measuring the SEE yield and backscattered electron coefficients in an SEM have been reported in literature by Reimer et al. [23] where a small, modified instrument was mounted on the specimen support of an SEM. The apparatus consisted of a spherical grid connected to ground and a spherical collector which is positively biased to + 50 eV so that the grid-collector combination prevents secondary electrons generated by backscattered electrons from leaving the collector. By applying a positive or negative bias on sample under consideration, the backscattered coefficient and SEE yield coefficients were calculated by measuring current at the collector. Previous work however does not make use of SEM imaging of the sample surface while in this paper, we present simultaneous SEE and complex surface morphology property evaluations by producing SEM images.

In this paper, we demonstrate the use of SEM for the evaluation of surface morphology and SEE properties from carbon velvet. Rather than directly measuring collector current, the pixel intensity of an SEM image is calibrated with planar graphite to estimate SEE yield and directly

compared with geometrical properties of the sample surface which are also determined by the SEM image itself. The dependence of SEE yield on the length of the carbon velvet fiber, fiber packing density, and fiber orientation is compared with recent theoretical results [9] and experimental results obtained using a conventional method for characterization of SEE properties with the electron gun and a collector of secondary electrons [10]. This method of SEE determination by measuring primary and secondary electron currents will be referred to as the direct SEE method. The details of this method are reported in Ref. [24]: the solid angle of the first grid is 120° , and the collector efficiency was measured to be between 85 - 87%. The accepted energies for secondary electrons was between 0 eV and 50 eV, and for primary electrons was between 50 eV and 2 keV. In the SEM, the efficiency of the Everhart-Thornley detector based on the subtended solid angle is 80 – 82%, and the collector grid is also biased to 50 eV while the primary electron beam can be modulated between 500 eV and 40 keV for optimal SEM image quality. In both cases, a cosine distribution is assumed for emitted electrons. The main differences between the proposed and conventional methods is that the former can provide information on local morphology and chemical composition of the surface irradiated by the electron beam, while the conventional method can provide a direct measurement of the SEE yield for a lower range of electron energies. These energies can be between 50 eV and 2 keV while the SEM method typically should be kept at > 500 eV electron energies. The SEM method however has the advantage of a precise stage for translating and tilting samples which can be used for measurements of the yield dependence on the incident electron beam angle. Both techniques can be complementary for the characterization of SEE properties from complex surfaces.

II. SEM analysis of velvet samples

II-1. Measurement procedure

Surface morphology and SEE properties of five carbon velvet samples with different fiber lengths and fiber packing densities were characterized using a conventional Environmental Scanning Electron Microscope at the Princeton Research Institute for the Science and Technology of Materials (PRISM). The carbon velvet samples used in this research were the same as those described in Table 1 of Ref [10]. In particular, the samples have fiber lengths varying between 0.5 mm and 3.0 mm, and a fixed fiber diameter of $\sim 3.5 \mu\text{m}$. In each sample, the fibers are attached to a 25.4 mm diameter graphite substrate. The packing density of a sample is normally defined as the ratio of fiber area to the total sample area. For the samples under this investigation, the packing densities are indicated by the manufacturer to be between 0.8% and 4.0%. These values however refer to the case when the fibers are normal with respect to their substrate, and the fiber area is comprised of fiber tips only. The actual packing densities of the samples range from 60-90%. This is because the fibers are mostly misaligned, and the fiber side surfaces contribute to the total fiber area. The method for calculating the true packing density of the carbon velvets using SEM is described in Ref 10.

To estimate SEE yield using SEM images of the velvet surfaces, all five samples were introduced into the SEM vacuum chamber simultaneously. The beam-sample parameters such as beam spot size, working distance, brightness and contrast were kept fixed so that the acquired images could be compared in post-processing under the same conditions. The digital brightness and contrast were chosen by monitoring a live pixel intensity histogram of the image so that the dynamic range was always entirely included. The primary electron beam scanned at a rate of $8 \mu\text{s}$ per pixel and was focused to a $\sim 2 \text{ nm}$ spot size. The beam current was $\sim 10 \text{ pA}$ therefore the dosing was of $8 \times 10^{-17} \text{ C}$ per location. A planar HOPG graphite sample smoothed by a lathe and with a

square area of $5 \text{ mm} \times 5 \text{ mm}$ was also imaged together with the velvet samples. This is in order to establish the link between the image pixel intensity and the SEE yield for the reference flat surface with known SEE yield obtained in previous direct measurements conducted using the current-sample method [24].

In SEM measurements, the electron beam energy was set to 0.5 and 1 keV. A total of ten adjacent $\sim 1 \text{ mm} \times 1 \text{ mm}$ surface regions of each sample were imaged. Each velvet SEM image was then analyzed as an 8-bit greyscale array of pixel intensities. The average greyscale pixel intensity of each image was calculated using MATLAB. Because the SEM detector signal strength is proportional to the number of secondary electrons collected, pixels with black image indicate no SEE yield, and pixels with white image indicate the highest SEE yield for graphite which should correspond to SEE yield at very shallow angles of incidence. The average pixel intensity of the smooth graphite sample was set equal to the known SEE yield from a graphite sample at the normal incidence angle of primary electrons. For example, in Refs. 10 and 24, the SEE yield of 0.85 was measured for a smooth graphite surface at 0.5 keV primary electron beam energy and the SEE yield of 0.75 at 1.0 keV primary electron beam energy. Pixel intensities brighter and SEE yields larger than the planar values indicate increased angle of incidence with the primary electron beam [25]. Refs. 10 and 24 used the same HOPG graphite sample in their measurements. For our experiments, the conversion factors between an 8-bit gray-scale pixel intensity value to SEE yield at 0.5 keV and 1.0 keV primary energies were respectively 0.0058 and 0.0043. For each SEM image, this factor was used to determine a qualitative estimate of SEE yield obtained in SEM measurements at the same beam energies. This process was repeated for each primary electron beam energy and therefore each primary energy measured produced a different conversion factor.

Figure 1 shows an example of a velvet surface imaged with 0.5 keV and 1.0 keV primary electron beam energies.

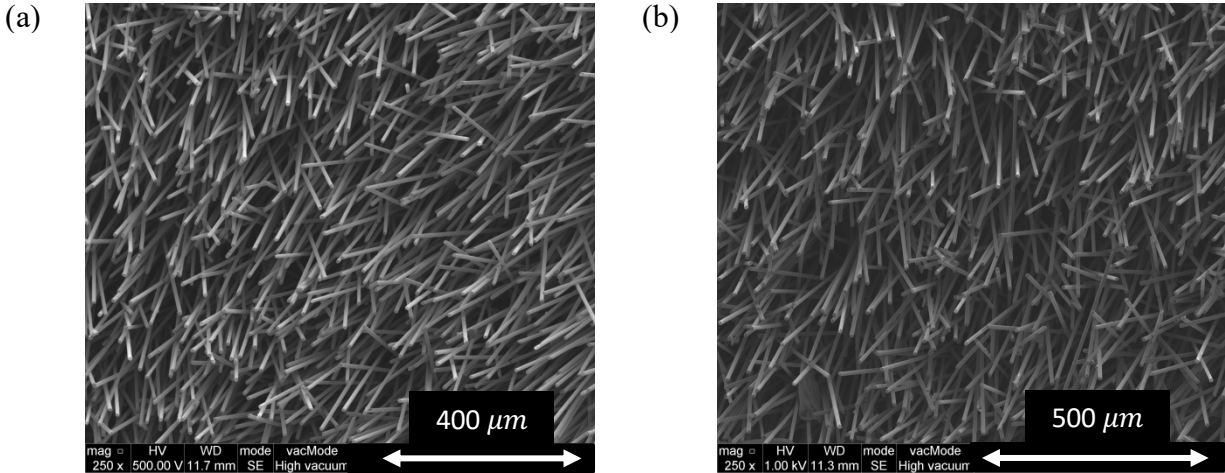


Fig. 1 (a) SEM image of carbon velvet with 0.5 mm fiber length and a manufacturer specified packing density of 4.0 %. The primary electron beam energy is 0.5 keV, and the actual packing density of the imaged region is 86%. (b) SEM image of the same sample using a primary electron beam energy of 1.0 keV. The actual packing density of this region is 92%.

II-2. SEM evaluation of samples morphology

SEM images were post-processed to estimate the average tilt angle of the fibers, θ , from their graphite substrate, and the actual packing density of the samples [10]. The tilt angles of the fibers were determined using SEM stereo-microscopy [26-27]. To apply this method, the same fiber surface was imaged twice: once with the sample stage at a normal angle to the primary electron beam, and once with a small eucentric tilt of $\alpha = 3^\circ$. These two images constitute a *stereopair*. During sample tilting, surface features with different heights will have different lateral displacements. Therefore, by tracking distinguishable features of the velvet fibers such as, for example, a fiber tip and its displacement with the known stage tilt angle and the fiber length, one

can deduce the inclination angle of the tilted fiber to the surface (azimuthal or tilt angle), θ . Figure 2 (a) shows a diagram of a fiber represented by the segment \overline{OB} . When titled, the same fiber is represented by the segment $\overline{OB'}$. A and A' are the fiber tip projections onto the plane imaged by SEM. The sum of angles α and θ is the total azimuthal fiber angle retrieved by the stereo-imaging method. Figure 2 (b) is an anaglyph made of the SEM stereopair which shows the lateral displacement between fiber tips (segment $\overline{AA'}$). The geometric calculations relating these quantities to solve for θ using the known fiber length and diameter are described in Appendix I.

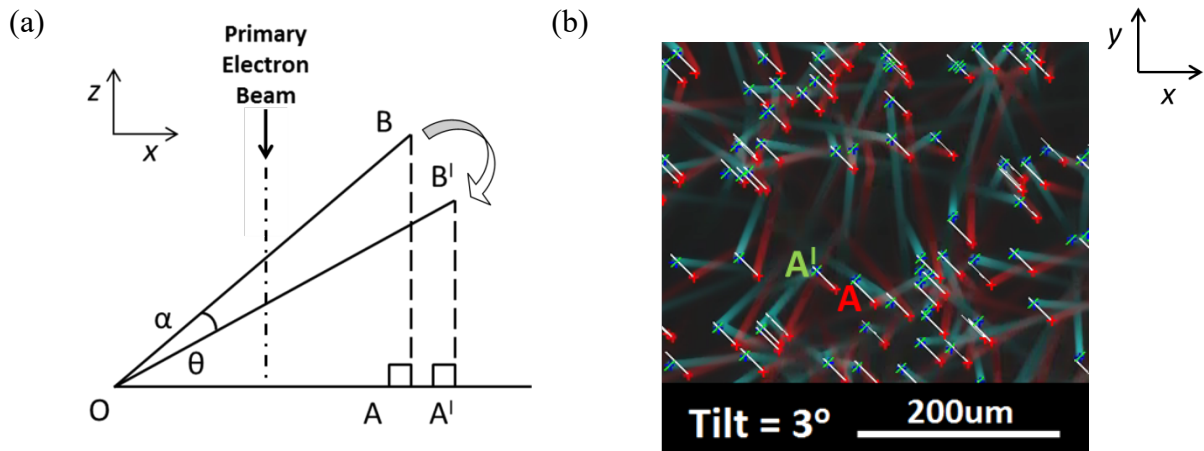


Fig. 2 (a) Diagram of a single fiber represented by segments \overline{OB} before tilting, and $\overline{OB'}$ after tilting. The distance $\overline{AA'}$ is found with an anaglyph as shown in (b) and it is proportional to the fiber height from the graphite base, segment \overline{BA} . (b) A carbon velvet anaglyph composed of a non-tilted image (red) and an image tilted by 3° (blue) with respect to the PE beam in the direction towards the SEE detector. This sample has fiber length of 1.5 mm and an actual packing density of 68%.

In order to accurately implement this method all SEM parameters including the magnification, the beam spot size, the electron beam energy and working distance were kept fixed for all acquired SEM stereopair images. A feature-matching algorithm was applied to the acquired

stereopairs in post processing using MATLAB to measure the displacements $\overline{AA'}$ from Fig. 2 (b) and to subsequently retrieve the individual azimuthal fiber tilt angles, θ . The average azimuthal angles of three velvets each with fiber length of 1.5 mm were calculated (Table I). Four stereopairs per sample were used to make these estimates. The uncertainty indicated in the table is due to the large spread in individual fiber misalignment.

Table I. Average azimuthal fiber angle properties for samples with 1.5 mm fiber length.

Manufacturing Packing Density [%]	Actual Packing Density [%]	Average Azimuthal Fiber Angle θ [°]
3.5	81 ± 6	20.0 ± 2
1.8	68 ± 5	25.2 ± 2
0.8	63 ± 3	30.9 ± 2

III. Results and discussions

III-1. Effect of local actual packing density on SEE yield

The SEE yield and actual packing densities of five carbon velvet samples were measured via SEM imaging. The average SEE yield was calculated using the pixel intensity calibration method with planar graphite as described in Sec. II-1. Figure 3 shows the dependence of the average SEE yield on the fiber packing density for multiple regions across each sample surface. Results show that the local SEE yield across a velvet surface is linearly related to the local actual packing density. This suggests that for velvet samples with actual packing densities in the range of 55 - 97% and fiber lengths of 0.5 – 1.5 mm, there is an increasing dependence of the SEE yield on the total amount of fiber surface area exposed to the incoming electron beam. At a primary electron beam energy of 0.5 keV, the percent increase in SEE yield with actual packing density for samples of 1.5 mm

fiber length are 33%, 19% and 23% corresponding to data in Figure 3 (b) – (d) respectively, and at 1.0 keV the percent increase in SEE yield with actual packing density for the same samples is 56%, 47% and 14%. Other samples demonstrate a similar trend at both primary electron beam energies. The errorbars in Figure 3 (a) are much smaller than the errorbars in rest of Figure 3 due to a small variation in fiber orientation for that sample. Figure 3 (a) corresponds to the velvet sample with the shortest fibers (0.5 mm). SEM imaging revealed that taller fibers tend to be more misaligned and therefore more susceptible to bunching and bending, causing more variation in actual packing density across the sample surface. The sample with 0.5 mm length fibers has a more uniform arrangement of fiber than other samples and the smallest variations in actual packing density and SEE yield.

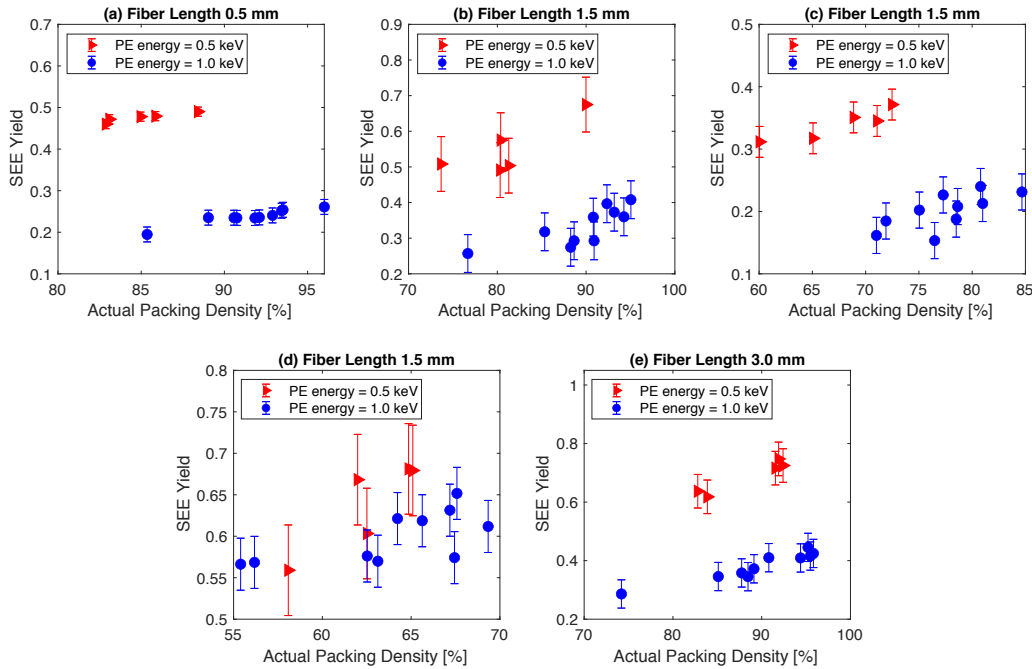


Fig. 3 SEE yield measured from SEM shown as a function of actual packing density for five carbon velvet samples using a primary electron beam energy of 0.5 keV (red markers) and 1.0 keV (blue markers). Each data point represents one SEM image analyzed for its actual packing density and SEE yield.

III-2. Effect of actual packing density on SEE yield

Figure 4 shows the effect of the actual packing density on the SEE yield measured for samples each with fiber length of 1.5 mm. The average SEE yield value was obtained by taking the mean average of multiple adjacent SEM measurements for each of the samples under analysis. While each data point in Figure 3 represents one SEM image at one location across the sample surface, the data points in Figure 4 are the average of all images for three different samples. These SEM results are also compared with recent SEE yield measurements of the same samples [10] and with values found by using recent models of SEE yield from velvet surfaces [9]. The theoretical values were calculated using Eq. 25 from Swanson et al.'s model in Ref 9. The model uses velvet aspect ratio, fiber density and angle from normal, θ , to compute a SEE yield of a carbon velvet surface from a 0.5 keV primary electron energy beam. The fiber angles found via stereomicroscopy (Table I) were used for θ in the model, and the resulting SEE yields are shown in Figure 4.

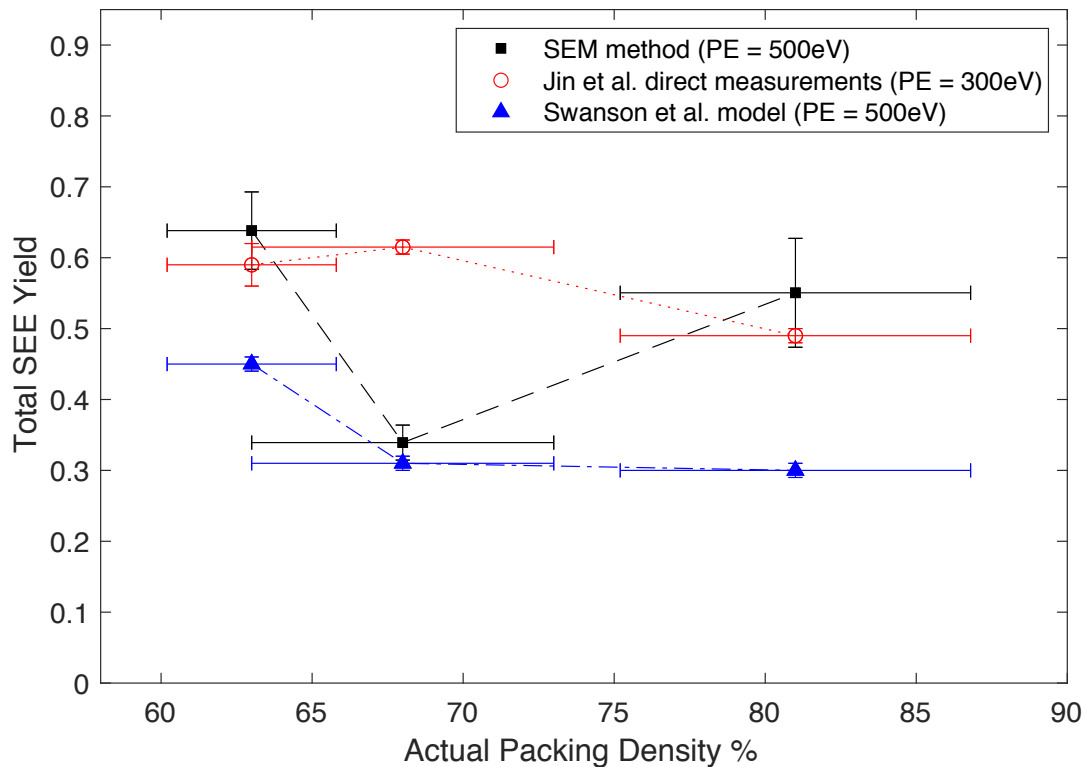


Fig. 4. SEE yield shown for three samples of 1.5 mm fiber length. The primary electron (PE) beam energy is 0.5 keV for the SEM method results (red circles), 0.3 keV for the experimental results (blue triangles), and 0.5 keV for the modeling results (black squares). The data points representing the SEM data are mean averages of 10 surface regions per sample.

The SEM results suggest that there is an optimal actual packing density at ~68% for a 1.5 mm long velvet surface. The trend of SEE reduction between a 63% ($\theta = 30.9^\circ$) and a 68% ($\theta = 25.2^\circ$) velvet surface is consistent in the SEM data and the modeled results. This optimal configuration suggests that the SEE yield depends not only of the fiber packing density, but also on the orientation of the fibers with respect to the graphite substrate. At the same time, the orientation depends also on the packing density as neighboring fibers may support each other. Thus, for the same fiber length there is a non-linear effect of the packing density of the SEE yield. This explains the optimum packing density and fiber length found in Figure 4.

Note that the above results are not in agreement with all direct electron gun measurements for the same samples. In particular, the SEE from the sample with a 68% packing density is the largest with an average SEE yield of 0.39, while in SEM it is the smallest with an average SEE yield of 0.64. This may be due to the fact that the spot size of the SEM beam is focused to ~10 nm in diameter while the spot size of the electron beam in the direct SEE experiments is 2-3 mm in diameter. Thus, in these SEM experiments, the results are given for different actual packing densities rather than for one averaged density value across an entire sample surface. With respect to Ref 10, the SEM measurements are much more localized because with SEM it is possible to observe exactly where the electron beam is pointing at on the sample. Good agreement between the SEM image data and the direct SEE current measurement is found for the actual SEE yield values of the velvet sample with 63% fiber density and the velvet with 81% fiber density. For these

cases the direct measurements and the SEM measurements are respectively within 8.2% and 10.9% of each other.

III-3. Effect of fiber length on SEE yield

To investigate the effect of fiber length on total SEE yield, three samples of varying fiber length and of similar actual fiber densities between 85% and 89% were compared (Fig 5 a). It is found that fiber length increases the total SEE yield of these samples. Swanson et al. recently developed an analytical model to describe the SEE yield of a velvet surface as a function of fiber length and of packing density (Eq. 25 in Ref. 10). An approximation of this model was used to describe the SEE yield of a velvet surface and then compared with the SEM measurements.

The approximation uses an outgoing particle flux equation to calculate the SEE yield (γ) of a velvet surface. The flux of secondary electrons outgoing from the graphite base of a velvet is attenuated due to the loss of these electrons to the fiber sides. The total rate of this attenuation is scaled by the packing density, D , and is expressed as $\frac{d\gamma(z)}{dz} \frac{1}{D}$. The corresponding flux term is defined as $-\gamma L$ where L is the fiber length. SEE generated from the fiber tips are not trapped and therefore they add to the total outgoing flux. This flux term is defined as $D\gamma_{flat}$ where γ_{flat} is the SEE yield from a fiber tip which is the same as the SEE yield from a flat graphite surface. The sum of these two terms define the change of the SEE yield as a function of depth from the graphite base, z :

$$\frac{d\gamma(z)}{dz} \frac{1}{D} = -\gamma(z)L + D\gamma_{flat} . \quad (1)$$

The solution to this differential flux equation is the exponential decay function:

$$\gamma(z) = c_1 e^{-Dz/L} + D\gamma_{flat} . \quad (2)$$

By applying the appropriate boundary conditions to Eq. (2), the quantity c_1 can be determined. At $z = 0$, the total SEE yield of the velvet surface should exclude SEE contributions from the fibers and should be equal to $(1-D)\gamma_{flat}$. This condition is satisfied when $c_1 = F(1 - 2D)$. When z instead approaches infinity, the SEE yield of the velvet surface should only be due to the fiber tips and be equal to DF . Equation (2) satisfies this condition as well. The exponential decay equation for the SEE yield of a fiber surface varying with fiber length in terms of fiber packing density and SEE yield of flat graphite is then:

$$\gamma(z) = (1 - 2D)\gamma_{flat} e^{-Dz/L} + D\gamma_{flat} . \quad (3)$$

In Figure 5 (a), the SEE yield of velvets measured with SEM with similar actual fiber densities are shown as a function of fiber length. The fiber length increases the SEE yield for velvets with actual fiber densities of 85 – 89%. In Figure 5 (b), the exponential decay approximation (Eq. (3)) to Swanson et al's model shows the opposite trend: SEE yield is reduced for velvets of increasing fiber lengths. SEE yield attenuation however is shown for packing densities which are much smaller than the actual densities found with SEM measurements (0.8 – 4.0%). For very large values of D , the expression approaches the value of γ_{flat} . The SEM measurements show that for actual fiber densities $> 75\%$, increasing fiber length may not attenuate SEE yield.

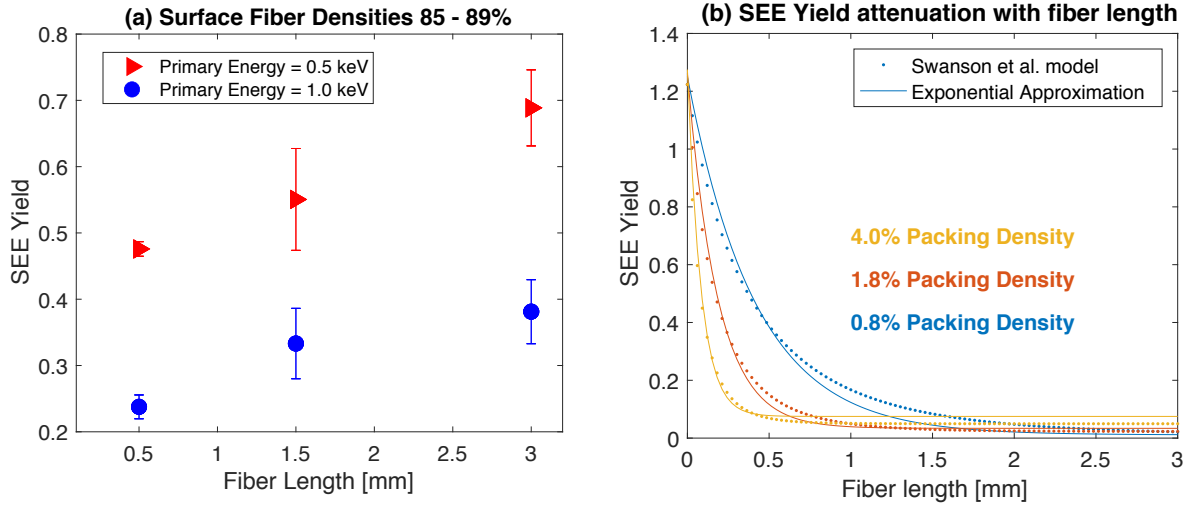


Figure 5 (a) SEE Yield plotted with fiber length for. (b) Eq. (3) exponential approximation function and the Swanson et al. SEE yield model shown for fiber packing densities between 0.8 and 4.0 % as a function of fiber length.

The increased SEE yield with increasing fiber length shown in Figure 5 (a) could be due to the realistic and non-uniform fiber arrangements revealed by SEM imaging of the velvet surfaces. For example, longer fibers in velvets with large packing density may tend to bend over and bunch more so than short fibers. The bent over fibers will then create regions where the primary electrons have shallow angles of incidence. Shallow incidence angles increase the SEE by an amount proportional to the inverse cosine law [28].

IV. Conclusions

To characterize SEE from complex surfaces, it is important to know the local morphology of the surface especially in the case where the surface is spatially non-uniform. This is difficult to achieve

using conventional direct SEE measurements. To this end, a method of using SEM imaging on carbon velvet surfaces has been proposed, demonstrated and validated for the simultaneous evaluation of the morphological features and SEE yield properties a velvet surface. It is shown that the method allows to correctly identify the key trends of SEE as a function of the actual packing density, fiber orientation and fiber length. In addition to using SEM for the SEE and morphological evaluation of a surface, the use of EDS incorporated with SEM can allow for the *in-situ* characterization of chemical compositions of spatial locations across a sample surface.

With respect to conventional SEE measurement methods, the SEM technique is rapid and highly localized. This is particularly useful for surfaces where the manufacturing specifications of the material are different than the actual material configurations. For example, in the case of carbon velvets, SEM allows to identify that the actual packing densities are up to 91% larger than the packing densities specified by the manufacturer. This is due to fiber bending and to non-uniform fiber alignment. By using SEM on the same velvet samples measured in Ref 10, it was also shown that a single velvet surface may have local SEE variation of up to 43%. A weak increasing trend was found for all velvet samples between local actual packing density and local SEE yield. These realistic surface configurations have also been shown to affect the SEE trends with respect to theoretical predictions.

The method of using SEM for a surface geometry and SEE evaluation on carbon velvets may be applied in the future to other conducting surfaces of high aspect ratio (>100), such as fractal feathered carbon velvets [11], surfaces with deep grooves or micro-foam structures.

ACKNOWLEDGEMENTS:

This was supported by US AFOSR. The authors are grateful to Drs. Charles Swanson, Igor Kaganovich, Chenggang Jin, Kimberly Cook-Chennault, Professor Sergey Prikhodko for fruitful discussions and to Professor Richard Wirz for his support.

APPENDIX I

The geometric representation shown in Figure 2 (a) is for a velvet fiber before tilting the SEM stage (\overline{OA}) and after tilting the SEM stage ($\overline{OB'}$) by an angle α . The distance $\overline{AA'}$ can be found by stereo microscopy image processing techniques using the two-dimensional SEM micrographs where the fibers are viewed in the x-y plane and \overline{BA} is measurable as shown in Figure 11 (b). Then $\overline{B'A'}$ can be derived as [26]:

$$A'B' = \frac{OA' \cos(\alpha) - OA}{\sin(\alpha)} \quad A1$$

and for small angles α

$$A'B' = \frac{AA'}{2 \sin(\alpha/2)} \quad A2$$

$$\text{Then } \theta = \arcsin\left(\frac{AA'}{L \cdot 2 \sin(\frac{\alpha}{2})}\right) \quad A3.$$

and the original fiber angle is $\theta + \alpha$ (from substrate).

REFERENCES

1. Y. Raitses, I. D. Kaganovich Electron Emission from Nano- and Micro- Engineered Materials Relevant to Electric Propulsion 33rd International Electric Propulsion Conference 390, 2013.
2. S. Mazouffre, S. Tsikata, and J. Vaudolon, *J. Appl. Phys.* 116, 243302 (2014).
3. S. I. Krasheninnikov, A. Y. Pigarov, and W. Lee, *Plasma Phys. Control. Fusion* 57, 044009 (2015).
4. F Subba, D Tskhakaya, Including the effect of secondary-electron emission at the divertor targets in code modelling, *Plasma Physics and Controlled Fusion* Volume 44, Number 1 (2001)
5. Hobbs G D and Wesson J A 1967 Heat flow through a Langmuir sheath in the presence of electron emission *Plasma Phys.* 9 85–7
6. Sydorenko D, Smolyakov A, Kaganovich I and Raitses Y 2006 Kinetic simulation of secondary electron emission effects in Hall thrusters *Phys. Plasmas* 13 014501
7. IJ. R. M. Vaughan, Multipactor, *IEEE Trans. Electron Devices* 35, 1172-1180 (1988).
8. Kato S and Nishiwaki M 2003 Secondary electron emission from metals and graphites Accelerator Tech. Design Report for J-PARC (11 March 2003) Y Yamazaki et al (Japan Atomic Energy Research Institute and High Energy Accelerator Research Organization) pp 2.3.8–7
9. C. Swanson, I. Kaganovich, Modeling of Reduced Effective Secondary Electron Emission Yield from a Velvet Surface, *Physics of Plasmas* 1607, 2016.
10. C. Jin, A. Ottaviano, Y. Raitses, Secondary electron emission from high aspect ratio carbon velvet surfaces *Journal of Applied Physics*, Vol 122, 2017.
11. C. Swanson, I. Kaganovich, “Feathered” fractal surfaces to minimize secondary electron emission for a wide range of incident angles, *Journal of Applied Physics* Vol 122 (2017).
12. M. Patino, Y. Raitses, and R. Wirz, Secondary electron emission from plasma-generated nanostructured tungsten fuzz, *APPLIED PHYSICS LETTERS* 109, 201602 (2016)
13. Patino M I, Raitses Y, Koel B E and Wirz R E 2013, Application of Auger spectroscopy for measurement of secondary electron emission from conducting material for electric propulsion devices Proc. 33rd Int. Electric Propulsion Conf. (Washington, DC, USA, 6–10 October 2013) pp 1–8
14. A. Ottaviano, C. Jin, S. Banerjee, Y. Raitses, “Characterization of secondary electron emission yield from velvet-type surface”, *International Electric Propulsion Conference – 195*, Atlanta, GA (2017)

15. J. M. Millet, J-P J. Lafon Secondary-electron emission from porous solids *Physics Review Letters A* 52, 1995.
16. M. Ye, Y. N. He, S. G. Hu, R. Wang Suppression of secondary electron yield by microporous array structure *J. Applied Physics* 113 074904, 2013.
17. M. T. F. Pivi, R. E. Kirby Sharp Reduction of the Secondary Electron Emission Yield from Grooved Surfaces *Journal of Applied Physics Vol* 104, 2008.
18. Goldstein, J., Newbury, D.E., Joy, D.C., Lyman, C.E., Echlin - *Scanning Electron Microscopy and X-ray Microanalysis*. Third Edition. (1998)
19. L. Reimer, “Image formation in Low-Voltage Scanning Electron Microscopy” (springer-verlag, Berlin 1985)
20. Drescher H, Reimer L, Seidel H: Rückstreuoeffizient und Sekundärelektronenausbeute von 10–100 keV Elektronen und Beziehungen zur Raster-Elektronenmikroskopie. *Z angew Phys* 29, 331–336 (1970)
21. K. S. Sim, J. D. White, New technique for in-situ measurement of backscattered and secondary electron yield for the calculation of signal-to-noise ratio in a SEM *Journal of Microscopy* 217, 2005.
22. A: Dennison, et al., “Absolute Electron Emission Calibration: Round Robin Tests of Au and Polyimide,” Proc.14th Spacecraft Charging Tech. Conf., Space Research and Technology Centre of the European Space Agency (ESA/ESTEC), (Noordwijk, Netherlands, April 4-8, 2016)
23. L. Reimer, C. Tollkamp, “Measuring the Backscattering Coefficient and Secondary Electron Yield Inside a Scanning Electron Microscope” *Scanning Volume* 3, 35-39 (1980)
24. M. I. Patino, Y. Raitses, B. E. Koel Analysis of secondary electron emission for conducting materials using 4-grid LEED/AES optics *J. Applied Physics* 48 195204, 2015.
25. D. C. Joy and D. E. Newbury, “Advanced SEM imaging”, *AIP Conference Proceedings* 449, 653 (1998)
26. J. Xie “Stereomicroscopy: 3D Imaging of the Third Dimension Measurement” *Application Note Agilent Technologies*, 2011.
27. D. Samak, et al., 3D Reconstruction and Visualization of Microstructure Surfaces from 2D Images, *Annals of the CIRP Vol.* 56/1/ (2007).
28. Bruining H 1954 *Physics and Applications of Secondary Electron Emission* (London: Pergamon)